Schweizerischer Erdbebendienst
Service Sismologique Suisse
Servizio Sismico Svizzero
Swiss Seismological Service

ETH zürich

SITE CHARACTERIZATION REPORT

SBIF2: Birsfelden (BL) - Friedhof

Clotaire Michel, Manuel Hobiger, Donat Fäh

Last Modification: 9th April, 2019

Schweizerischer Erdbebendienst (SED)
Service Sismologique Suisse
Servizio Sismico Svizzero
Servizi da Terratrembels Svizzer

ETH Zurich
Sonneggstrasse 5
8092 Zurich
Schweiz
clotaire@sed.ethz.ch

Contents

Summary

Station SBIF2 is the replacement for dial-up station SBIF. It was moved 25 m away and installed in free-field. For the site characterization, an existing passive seismic array measurement was reprocessed. It allowed us to retrieve 1D velocity profiles at the station site. The site shows loose sediments with shear-wave velocities of around 200 m/s in the superficial 4 m, followed by unconsolidated sediments with velocities of about 500 m down to 17 m. Below, velocities increase until around 60 m of depth, where a velocity of about 900 m/s is found. A deep velocity contrast is modeled at around 240 m of depth, but the structure at these depths is not well constrained. $V_{s,30}$ is 440 m/s and the site corresponds to ground type B according to Eurocode 8 (CEN, 2004) and type C in SIA261 (SIA, 2014). The theoretical 1D SH transfer function computed from the inverted profiles shows a large amplification peak at about 14 Hz.

1 Introduction

In the framework of the second phase of the Swiss Strong Motion Network (SSMNet) renewal project, the dial-up station SBIF (Birsfelden (BL), Friedhof) was replaced by a modern free-field station (see Fig. 1) and was therefore moved 25 m to the west. The station is located in the Rhine Graben in Basel, close to the master fault marking the eastern end of this geological structure. The new station went operational on 4 November 2014.

Figure 1: Station SBIF2 in the cemetery of Birsfelden (BL).

2 Geological setting

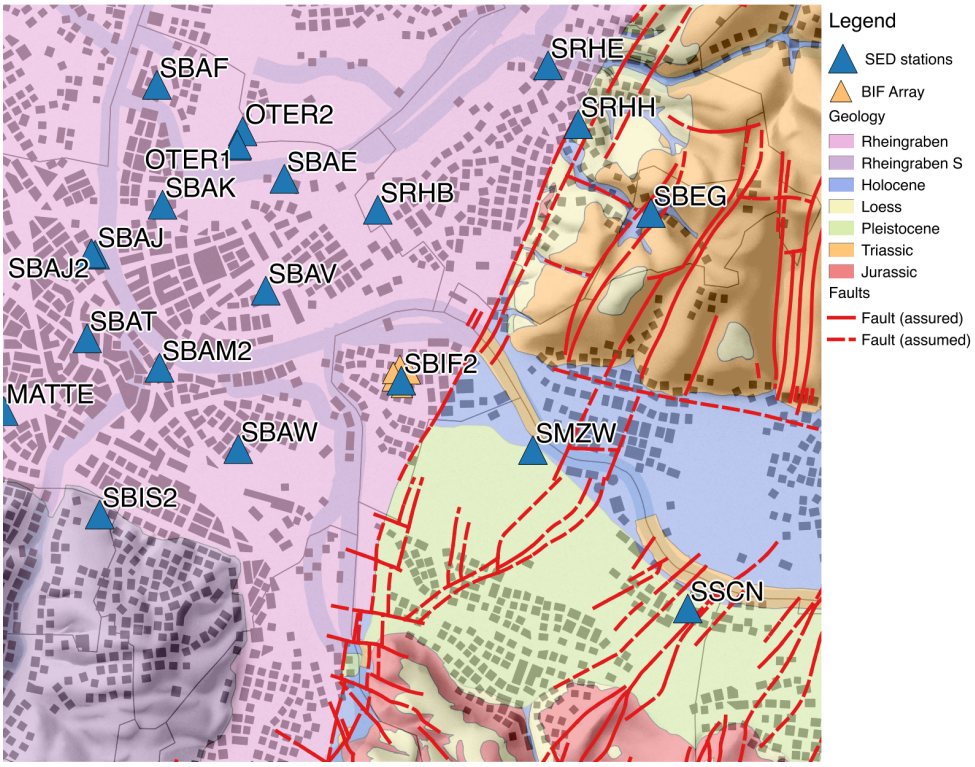

Figure 2: Simplified geological map of the Basel area around Birsfelden, superimposed on a relief map (data: ©2018 swisstopo JD100042). The SED stations are represented as colored triangles.

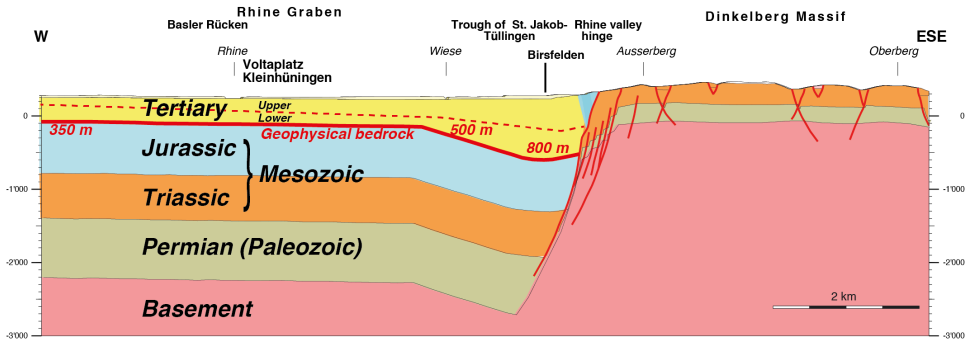

Figure 3: Geological W-E cross-section through the Rheingraben (modified from Michel et al. (2017)).

Michel et al. (2017) and Michel and Fäh (2016) described the geological context in Basel from an engineering seismology perspective. Station SBIF2 is located close to the deepest point of the Rhine graben (800-1000 m depth), close to the master fault of the graben. According to the available geological data, the soil column at SBIF2 is made of 15 to 20 m of Quaternary sediments (alluvia from the Rhine) overlaying the poorly consolidated Tertiary layers. The borehole BL-17.N.30, located few meters away from SBIF2, details the composition of the Quaternary layers, mostly made of gravels. The roof of the Tertiary (Tuellinger layer) is found at 17.2 m depth but the upper part is weathered. The

upper Tertiary (Oligocene age) is divided into the Niederroedern formation and the Froidefontaine formation. The Niederroedern formation can itself be divided into the Tuellinger layers (marls and limestone) and the Molasse alsacienne (maximum thickness of 300 m), made of marl, siltsone, sandstone and limestone of freshwater origin. SBIF2 is located at the eastern border, where the Tuellinger layer is present, i.e. probably with limited thickness.
The Froidefontaine formation (up to 400 m thickness) is made of the formerly called "Séries grises" (Cyrenenmergel, Septarienton – formerly known as Meletta layers or Blauer Letten – etc.), seawater sediments of Rupelian age, mostly made of mudstone (Septarienton formation). Below the Froidefontaine formation, the lower Tertiary (roof at 459 m depth according to the Basel geological model) is constituted by a first layer of marls (Pechelbronn formation formerly called Sannoisian, Bunte Mergel or Haustein). The upper Mesozoic layers in the graben are made of massive limestone of Oxfordian age. The roof of the lower Tertiary has been considered as the geophysical bedrock since the first studies on Basel. However, Michel and Fäh (2016) showed that the geophysical bedrock is located at the roof of the Mesozoic units. According to the GeORG data, the roof of the Mesozoic is located at about 660 m depth but is steeply dipping to the West.

According to the microzonation of Basel, the site is located in the zone Rheingraben Ost, in the sub-zone Holocene.

3 Site characterization using passive measurements

3.1 Measurements and data set

We reprocessed the passive seismic array measurements performed by H.-B. Havenith in February 2005. The layout of the seismic array is shown in Fig. 4.
The parameters of the array are given in Table 1. For this measurement, 7 Quanterra Q330 dataloggers named NR1 to NR7 and 7 Lennartz 3C 5 s seismometers were used. Each datalogger can record on the two ports A (channels EH1, EH2, EH3 for Z, N, E directions) and B (channels EH4, EH5, EH6 for Z, N, E directions). Time synchronization is ensured by GPS.
The sensor coordinates were probably measured using a theodolite. Three configurations made of rings of increasing radius around a central station had been performed.

Table 1: Characteristics of the seismic array measurements in Birsfelden.

Array name	Number of sensors	Minimum interstation distance [m]	Aperture [m]	Recording time [min]
BIF_Z1	7	20	40	28
BIF_Z2	7	50	110	26
BIF_Z3	6	95	230	36

The largest time windows, for which all sensors of the array were correctly placed and the GPS synchronization was ensured, were extracted. The recordings are short compared to the current practice. While the recordings are well correlated below 1 Hz, strong differences are noted for higher frequencies. Only few harmonic disturbances can be noted.
Orientations of the sensors were checked by maximizing the correlation with the central station at low frequencies (Poggi et al., 2012b). Corrections lower than 12 ° were generally performed except at points ASBIF_07 (19 °), ASBIF_16 (15 °) and ASBIF_17 (13 °).

Figure 4: Layout of the array measurements at site SBIF2. The array stations from the different configurations are in red to light orange and station SBIF2 in blue.

3.2 Single station measurement results

3.2.1 H/V curves

The H/V curves across the array are presented in Fig. 5. They all show a homogeneous peak at 0.42 Hz corresponding to the resonance of the Tertiary and Quaternary layers in the Rhine graben. The H/V curves are homogeneous until a frequency of 10 Hz, above which some peaks can be recognized, corresponding to few meters of unconsolidated sediments. The variability of these peaks is not different for the larger rings indicating that they are very local and won't be retrieved using the analysis of surface waves. The closest station to SBIF2 was ASBIF_10 where this peak is absent. Note that a well-known anthropogenic peak at 1.13 Hz is disturbing the H/V curves around this frequency value. Different methods to compute H/V ratios are compared for point ASBIF_00 in Fig. 6, the classical methods were divided by $\sqrt{2}$ to correct for the Love wave contribution (Fäh et al., 2001). The 3C FK analysis (Capon method) matches well with the H/V analysis (see section 3.3).
WaveDec (see section 3.4) for the Z2 and Z3 datasets shows lower values than the H/V analysis. The Z3 dataset processed with this technique shows a singularity at about 14 Hz, while the other techniques just display a small peak.
In conclusion, the fundamental peak at station SBIF2 is found at 0.42 Hz, with a peak amplitude of around 2.5 and the second peak at 14 Hz with a peak amplitude lower than 2 in the H/V but appearing to be a singularity according to the WaveDec analysis.

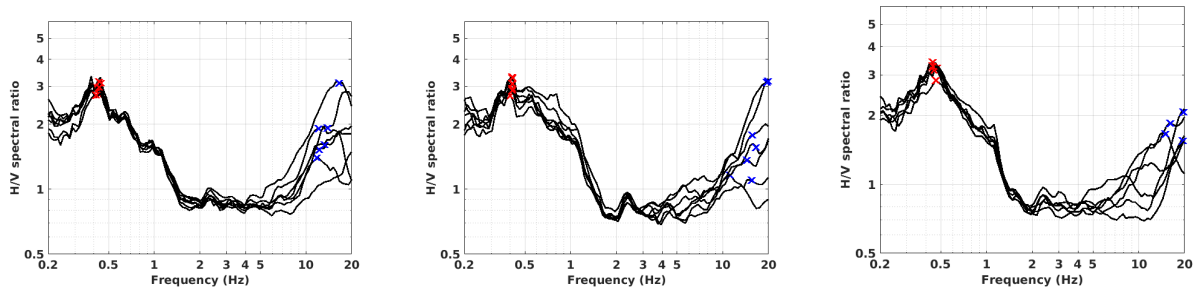

Figure 5: Comparison of H/V spectral ratios (time-frequency analysis code of V. Poggi) of the different points of the arrays. Left: Z1; centre Z2; right: Z3.

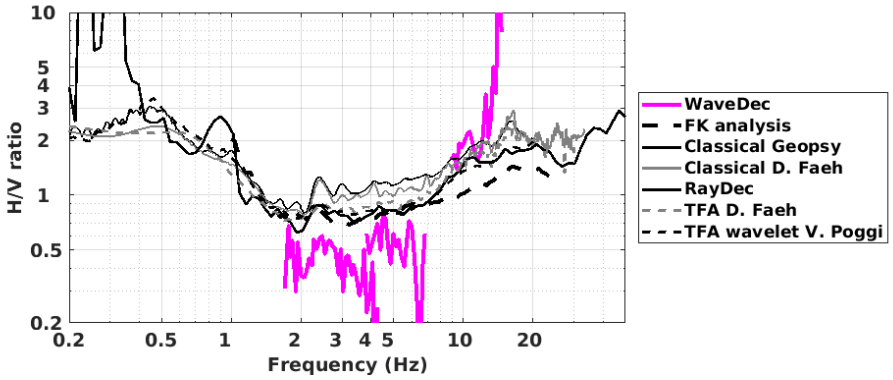

Figure 6: H/V spectral ratios for point ASBIF_00 using the different codes. Classical methods were divided by $\sqrt{2}$.

3.2.2 Polarization analysis

The polarization analysis on the array data was performed to check for 2D resonance using the method of Burjánek et al. (2010). The wavefield does not show any particularly elliptical motion in the direction of the axis of the graben (Fig. 7). The disturbing peak at 1.1 Hz, however, is polarized in the direction of its source (still mysterious). Therefore, 2D resonance can be excluded at this site.

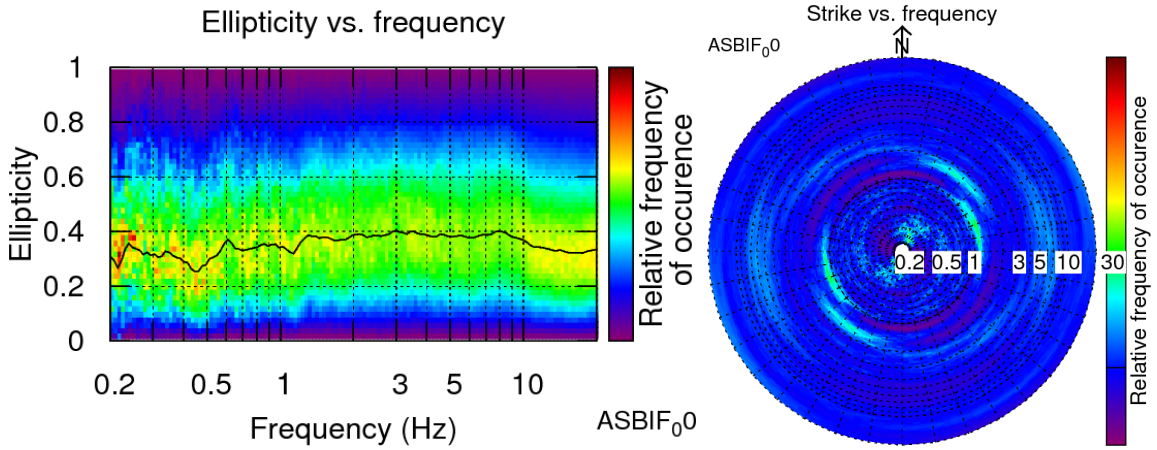

Figure 7: Polarization analysis at point ASBIF_00. Left: Ellipticity (A trough in the ellipticity corresponds to polarized motion). Right: Strike of the polarization.

3.3 1- and 3-component high-resolution FK

Fig. 8 shows the results of the 1C HRFK analysis using the Geopsy software. It shows a clear fundamental mode of Rayleigh waves between 2 and 15 Hz. The results of the 3-component HRFK analysis (Poggi and Fäh, 2010) are shown in Fig. 9. It should be noticed that in both cases, the picking was performed on the individual configurations, while all three datasets have been merged in Fig. 8 and Fig. 9. One can also notice that the recording is short, providing only a limited amount of data. The Rayleigh wave fundamental mode can be seen from the vertical component between 1.65 and 15 Hz, while the radial component does not show this mode. The Love wave fundamental mode is retrieved between 2 and 15 Hz on the transverse component.
The ellipticity curve determined with the 3-component HRFK analysis matches the H/V ratios (Fig. 6).

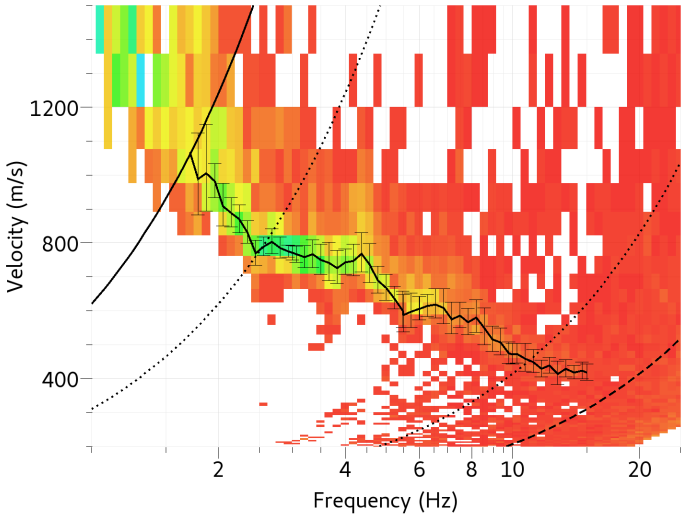

Figure 8: Dispersion curves obtained from the 1C HRFK analysis.

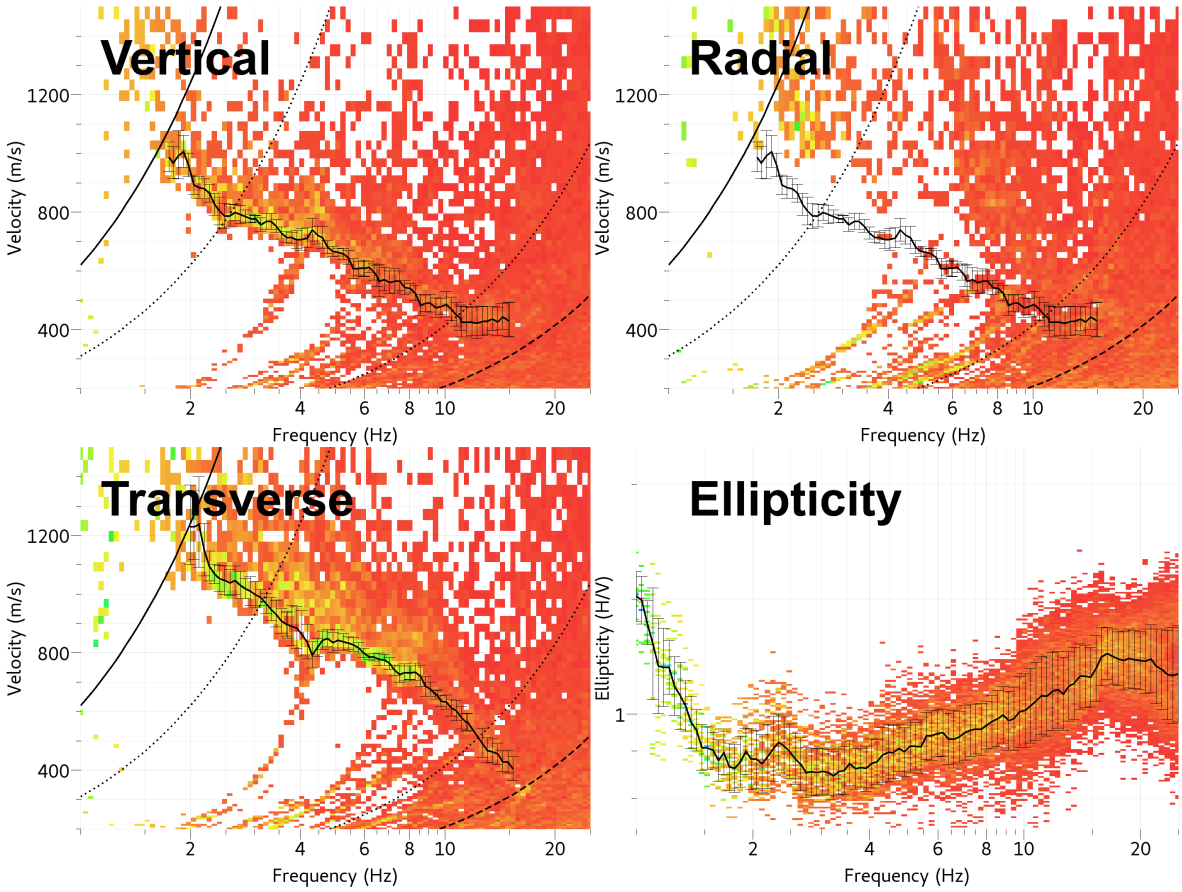

Figure 9: Dispersion curves obtained from the 3C HRFK analyses. Top row: Vertical and radial component; bottom row: transverse component and ellipticity. The picking is based on the analysis of each array dataset alone.

3.4 Wavedec

WaveDec (Maranò et al., 2012) has also been used to process the three datasets. This technique estimates the properties of multiple waves simultaneously with a maximum likelihood approach in the time domain. It was applied assuming the presence of 3 waves (Love and Rayleigh) with a γ value of 0.2 that penalises less the complexity and therefore may contain more noise.
The fundamental Love and Rayleigh wave dispersion curves could be picked within the array limits (Fig. 10) and are compared to the FK analysis in section 3.5. The ellipticity angle of Rayleigh waves (Fig. 11) shows retrograde waves (corresponding to neagtive ellipticity angles). A change in the sense of rotation from retrograde to prograde can be seen around 14 Hz (singularity).

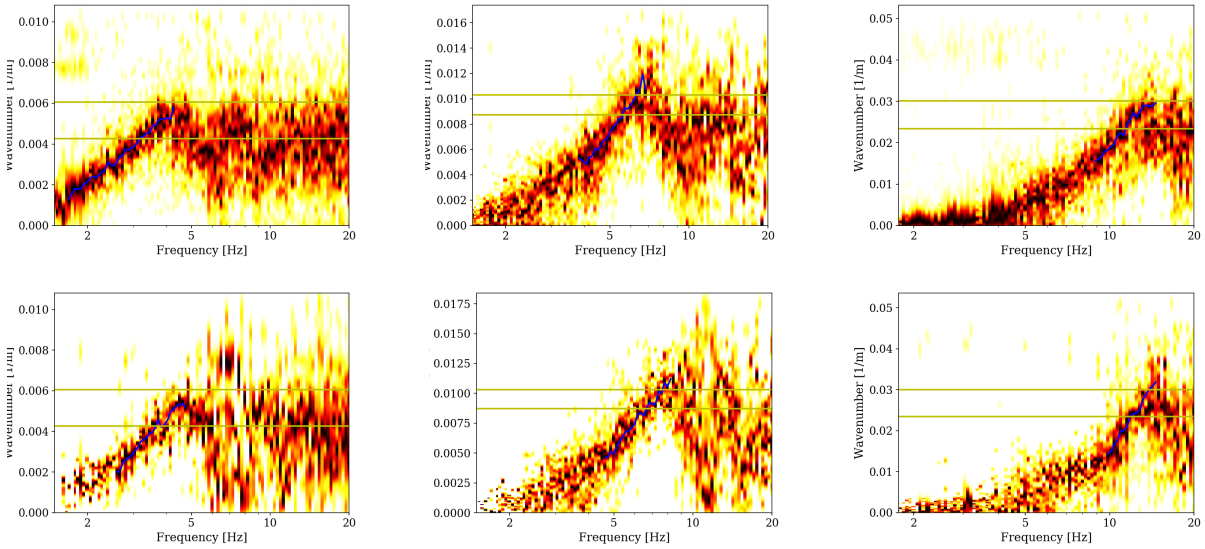

Figure 10: Rayleigh (top) and Love (bottom) wave dispersion curves obtained with the WaveDec technique (Maranò et al., 2012) for the datasets Z3 (left), Z2 (centre) and Z1 (right). The yellow lines indicate the theoretical array resolution limits.

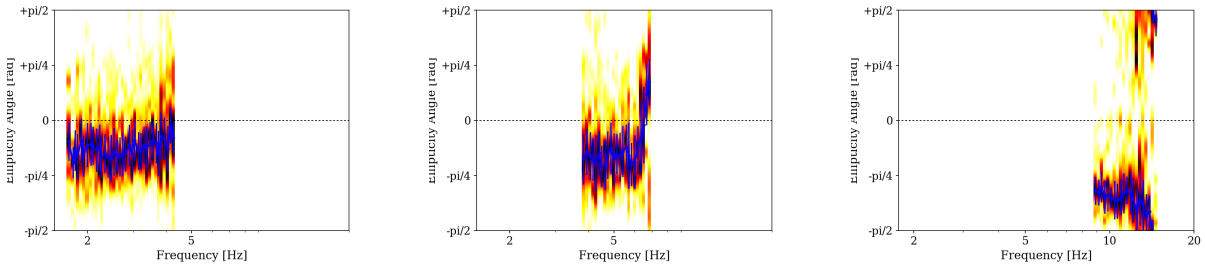

Figure 11: Ellipticity curve of the fundamental mode of Rayleigh waves with the WaveDec technique (Maranò et al., 2012).

3.5 Interpretation

Fig. 12 gives an overview of the dispersion curves determined with the different methods. The fundamental dispersion curve of Rayleigh waves was consistently retrieved by all methods. One noticeable deviation concerns the WaveDec analysis of the Z1 dataset, which shows higher phase velocities than the other methods. The obtained curves do not differ significantly from the one obtained by H.-B. Havenith in his 2006 report (black curve in Fig. 12), except that he underestimated the resolution limit and extended the curve to lower frequencies than reliable. Regarding high frequencies, the curve is not retrieved above 15 Hz where the H/V analysis showed a strong heterogeneity in the array. The fundamental mode of Love waves is also consistently retrieved using FK and WaveDec while it was not investigated in previous studies.

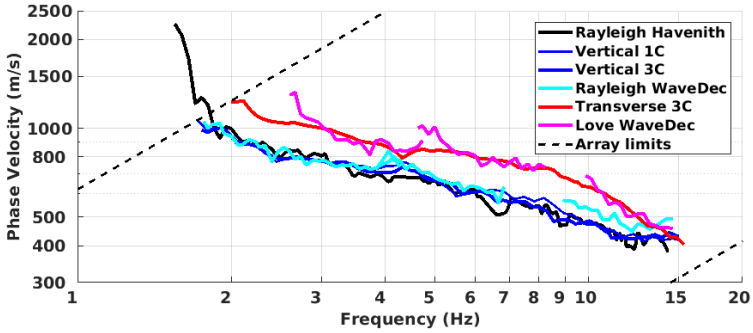

Figure 12: Picked dispersion curves from the 1C, 3C HRFK analyses, WaveDec and the existing curve from the database as picked by H.-B. Havenith.

As for many other arrays in Basel (e.g. SBAV, SBAW, SRER, SBAJ2, Kannenfeld, ...), the inversion shows that Love and Rayleigh curves are not compatible. Many tests have been performed in the past to assume a different mode assignment, a velocity reversal (Fäh et al., 2008), assumption of anisotropy (Michel and Fäh, 2016) and combinations of those. However, from the above plot, it is clear that a shift of 25% of Love wave dispersion curve allows to perfectly match Rayleigh waves dispersion. This is true on a broad frequency range which rules out anisotropy and velocity reversal. We tested the effect of systematic misorientation of sensors that affect the computed velocity of the horizontal components but it also has a complex effect that is not so broadband. More assignment could still be a solution, although the retrieved curve would be in between the fundamental and the first higher mode so mode mixing should be seen. The last option is the absence of Love waves and a failure of the decomposition of the horizontal components. What we see on the transverse component would therefore just be Rayleigh waves. For this reason, the Love wave dispersion curve is not trusted and not used in the inversion.

3.6 Data inversion

The inversion of the surface wave properties into 1D velocity profiles was performed using the Improved Neighborhood Algorithm (NA) (Wathelet, 2008) implemented in the Dinver software. In the inversion, 10000 starting models are used. 100 new cells are generated in the neighborhood of the 100 best cells (1 per cell) and 500 iterations of this process are performed. The process ends therefore with 60000 models explored.

3.6.1 Misfit function

The misfit function is based on the Rayleigh wave fundamental mode dispersion curve and the ellipticity curve based on the TFA analysis code of V. Poggi and WaveDec, with a weight of 0.1. The TFA curve is used between 0.5 and 10 Hz while the WaveDec curve of the Z1 dataset is used until 14 Hz (singularity) . It was not possible to constrain the deep part of the profile using the fundamental frequency of resonance due to the complex velocity setting as shown by the Otterbach borehole (Michel et al., 2017). All curves were resampled using 50 points between 0.2 and 20 Hz in log scale. No uncertainty was considered in the misfit function (all points with the same weight).

3.6.2 Parametrization of the model space

We assumed increasing velocity with depth because no velocity reversal is apparent in the data. Velocity reversals are known at greater depth than that explored (Michel et al., 2017) but could not be constrained with our data. Ground profiles until 300 m depth were explored. The Poisson ratio was inverted in the range 0.2-0.45 (up to 0.47 in the upper layers). The density was assumed to be 2000 kg/m^3 except in the lowest layer (2200 kg/m^3). Inversions with free layer depths as well as fixed layer depths were performed. 4 layers over a half-space are enough to explain the targets (dispersion and ellipticity), but more layers are used to smooth the obtained results and better explore the parameter space. 5 independent runs of 5 different parametrization schemes (5 and 6 layers over a half-space and 13 layers with 3 sets of fixed depths) were performed, i.e. a total of 25 runs.

3.6.3 Results

Examples of retrieved ground profiles for the different strategies are presented in Fig. 13. When comparing to the target curves (see Fig. 14 for an example with fixed layer depth, representative of the other computations), the dispersion curve is well reproduced. The ellipticity is reproduced, especially the high frequency singularity and the flat behaviour between 2 and 10 Hz. The retrieved models produce a fundamental peak around 1 Hz with too high values compared to the observation. While the low frequency peak at 0.42 Hz is definitely absent and can only be explained with a deeper profile, the retrieved small peak is not absurd when compared to the ellipticity (trough, small bump) and may be real, hidden by the large 0.42 Hz peak in the H/V curve. It should be noticed that it is driven by the dispersion curves, not the ellipticity curve alone. For further elaborations, the best models of these 25 runs were selected and used (see section 4.1).

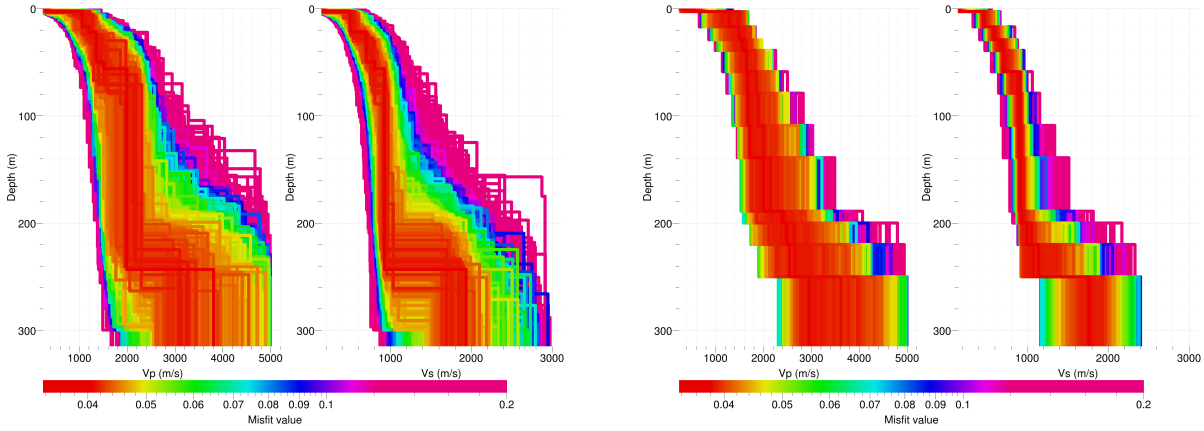

Figure 13: Inverted ground profiles at SBIF2 in terms of V_p and V_s using the free layer depth (6 layers – left) and the fixed layer depth (13 layers – right) strategies.

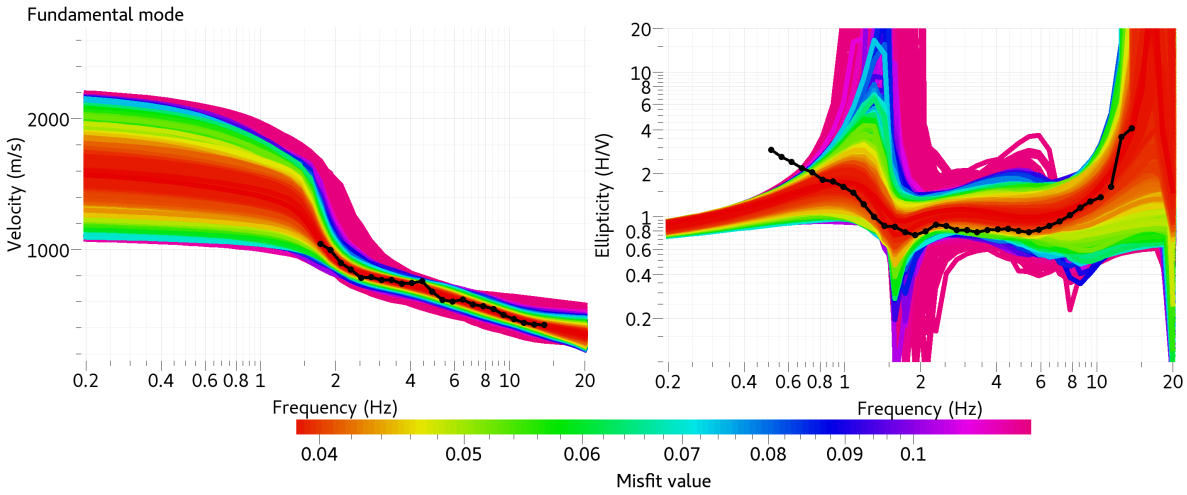

Figure 14: Comparison between inverted models and measured Rayleigh wave dispersion curve and Rayleigh wave ellipticity for the fixed layer inversion.

4 Interpretation of the velocity profiles

4.1 Velocity profiles

The profiles of the best models (Fig. 15) show low velocities of 150-200 m/s in the first 3-4 meters corresponding to loose surface sediments and responsible for the singularity between 10 and 15 Hz. A second layer of unconsolidated sediments (Quaternary) is found down to 17 m as shown by the boreholes, with a velocity of about 500 m. Below, the velocity of the upper Tertiary is regularly increasing up to 700 m/s at 30 m. This corresponds to weathered Molasse (Tuellinger layer) in the first 15 m, while below, this layer is weakly consolidated. Another interface is retrieved at around 60 m depth that makes the velocity increase to 900 m/s. It could be related to the limit between the Tuellinger layer and the Molasse alsacienne. The velocity is then constant down to the retrieved interface at about 240 m. Relating this interface to a geological interface is too speculative (interface between Molasse alsacienne and Froidefontaine formation for instance). The interface with the lower Tertiary is in any case much deeper (460 m according to the geological model). The velocity below this interface is not well constrained.
The Poisson ratio is found around 0.4 for the whole profile besides the lowest layer.
$V_{s,30}$ was computed for the different models and found to be 440 m/s, corresponding to ground type B in Eurocode 8 (CEN, 2004) and C in SIA261 (SIA, 2014).

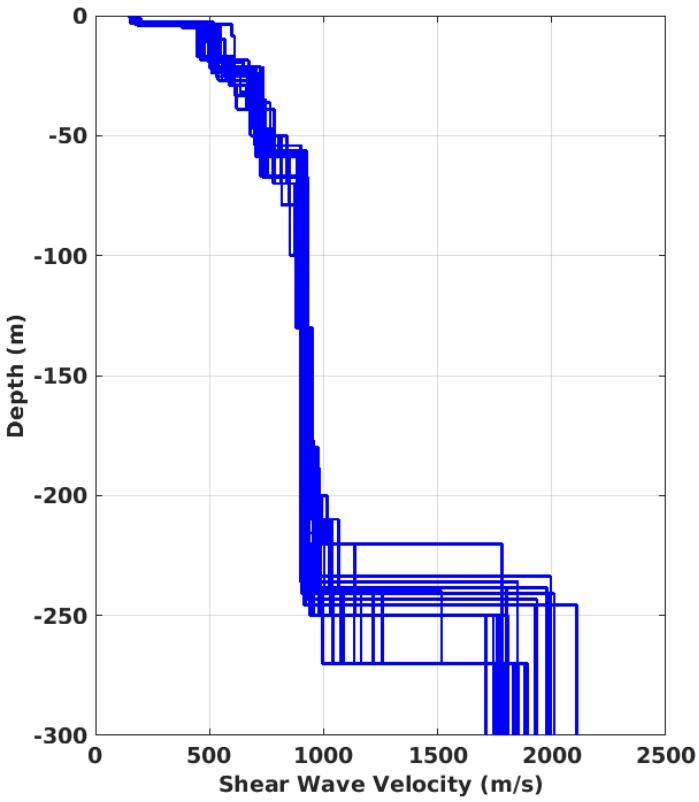

Figure 15: Shear-wave velocity profiles of the 25 selected models.

4.2 Quarter-wavelength representation

The quarter-wavelength velocity approach (Joyner et al., 1981) provides, for a given frequency, the average velocity at a depth corresponding to 1/4 of the wavelength of interest. It is useful to identify the frequency limits of the experimental data (minimum frequency in dispersion curves at 1.65 Hz and lowest value fitting in the ellipticity curve at 1 Hz). The results using this proxy show that the dispersion curves constrain the profiles down to 100 m and the ellipticity to 190 m (Fig. 16). Moreover, the quarter wavelength impedance-contrast introduced by Poggi et al. (2012a) is also displayed in the figure. It corresponds to the ratio between two quarter-wavelength average velocities, respectively from the top and the bottom part of the velocity profile, at a given frequency (Poggi et al., 2012a). It shows a trough (inverse shows a peak) at the resonance frequency.

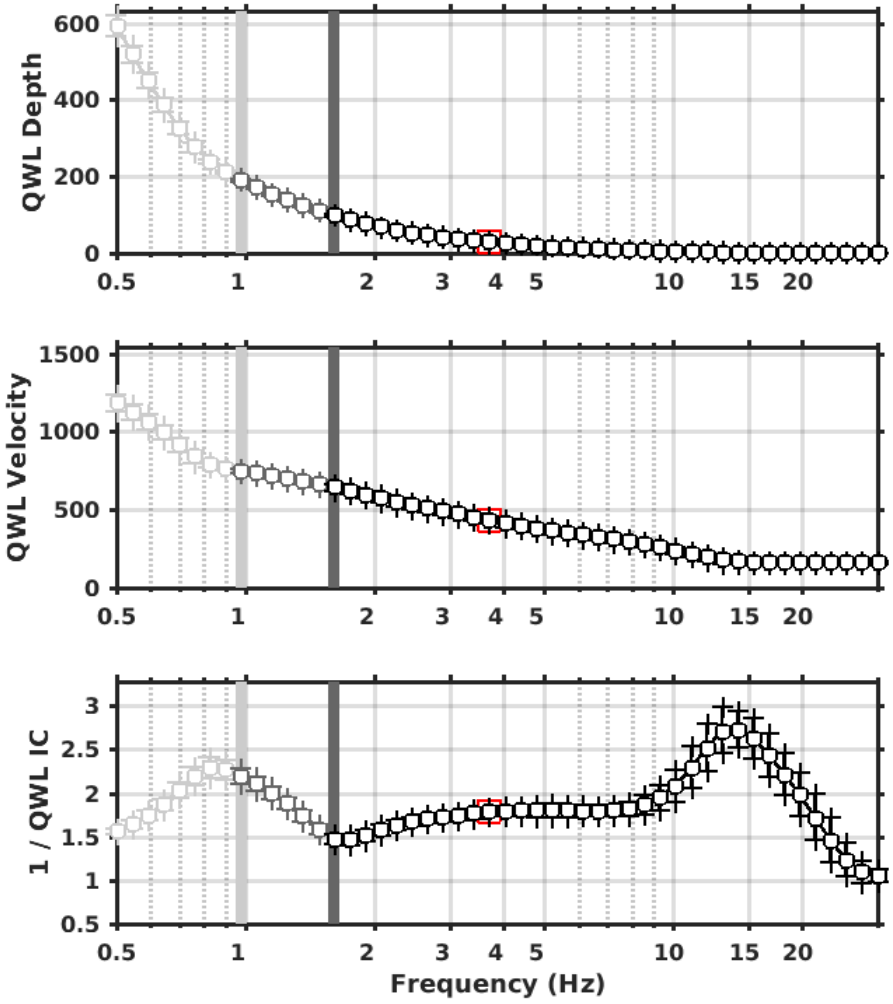

Figure 16: Quarter wavelength representation of the velocity profile for the selected velocity profiles (top: depth, center: velocity, bottom: inverse of the impedance contrast). The black curves are constrained by the dispersion curves, the light grey curves are not constrained by the data. The red square corresponds to V_{S30}.

4.3 SH transfer function

The theoretical SH-wave transfer function for vertical propagation (Roesset, 1970) is computed from the selected profiles. It is corrected with respect to the Swiss Reference Rock model (Poggi et al., 2011) following Edwards et al. (2013). It shows small peaks from 1 Hz and a larger one at 14 Hz, reaching an amplification of 4 (Fig. 17). It is compared to the amplification function obtained by empirical spectral modelling (ESM) (Edwards et al., 2013; Michel et al., 2014, 2017). The discrepancy at low frequencies is expected. Some of the intermediate peaks are somehow reproduced. The large peak at 14 Hz, however, seems to occur at 11 Hz but it also corresponds to the upper bound of the part with a sufficient amount of data in the ESM and it seems to correspond to a signal of anthropogenic origin.

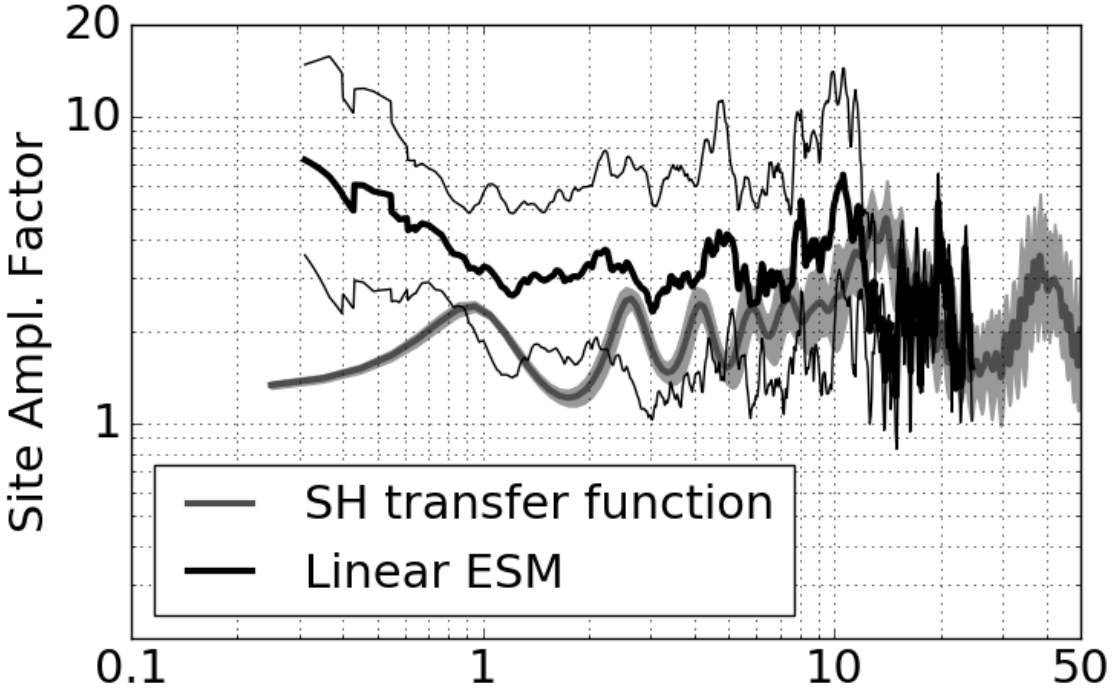

Figure 17: Comparison between the modeled SH transfer function for the selected velocity profiles and the empirical amplification (ESM) measured at station SBIF2 (with standard deviation).

5 Conclusions

The passive measurements presented in this study were successful in deriving a velocity model for the site SBIF2. The profiles show 3 to 4 m of loose sediments with shear-wave velocities of around 200 m/s, followed by unconsolidated sediments with velocities of about 500 m down to 17 m. Below, the upper Tertiary with velocities increasing to 700 m/s is found. At around 60 m of depth, the velocity increases to about 900 m/s. A deep velocity contrast is modeled at around 240 m of depth, but the structure at these depths is not well constrained. The 4 m-interface creates the high-frequency resonance peak beteen 10 and 15 Hz, the fundamental resonance frequency of around 0.42 Hz would correspond to the deep interface which is not well retrieved.
$V_{s,30}$ is 440 m/s and the site corresponds to ground type B according to Eurocode 8 (CEN, 2004) and type C in SIA261 (SIA, 2014). The theoretical 1D SH transfer function computed from the inverted profiles shows a large amplification peak at about 14 Hz.

Acknowledgements

The authors thank Hans-Balder Havenith who performed the measurement.

References

Burjánek, J., Gassner-Stamm, G., Poggi, V., Moore, J. R., and Fäh, D. (2010). Ambient vibration analysis of an unstable mountain slope. *Geophysical Journal International*, 180(2):820–828.

CEN (2004). *Eurocode 8: Design of structures for earthquake resistance - Part 1: General rules, seismic actions and rules for buildings*. European Committee for Standardization, en 1998-1: edition.

Edwards, B., Michel, C., Poggi, V., and Fäh, D. (2013). Determination of Site Amplification from Regional Seismicity : Application to the Swiss National Seismic Networks. *Seismological Research Letters*, 84(4).

Fäh, D., Kind, F., and Giardini, D. (2001). A theoretical investigation of average H/V ratios. *Geophysical Journal International*, 145(2):535–549.

Fäh, D., Stamm, G., and Havenith, H.-B. (2008). Analysis of three-component ambient vibration array measurements. *Geophysical Journal International*, 172(1):199–213.

Joyner, W. B., Warrick, R. E., and Fumal, T. E. (1981). The effect of Quaternary alluvium on strong ground motion in the Coyote Lake, California, earthquake of 1979. *Bulletin of the Seismological Society of America*, 71(4):1333–1349.

Maranò, S., Reller, C., Loeliger, H. A., and Fäh, D. (2012). Seismic waves estimation and wavefield decomposition: Application to ambient vibrations. *Geophysical Journal International*, 191(1):175–188.

Michel, C., Edwards, B., Poggi, V., Burjánek, J., Roten, D., Cauzzi, C., and Fäh, D. (2014). Assessment of Site Effects in Alpine Regions through Systematic Site Characterization of Seismic Stations. *Bulletin of the Seismological Society of America*, 104(6):2809–2826.

Michel, C. and Fäh, D. (2016). Basel Earthquake Risk Mitigation Computation of scenarios for school buildings. Technical report, ETH-Zürich, Zürich, Switzerland.

Michel, C., Fäh, D., Edwards, B., and Cauzzi, C. (2017). Site amplification at the city scale in Basel (Switzerland) from geophysical site characterization and spectral modelling of recorded earthquakes. *Physics and Chemistry of the Earth, Parts A/B/C*, 98:27–40.

Poggi, V., Edwards, B., and Fäh, D. (2011). Derivation of a Reference Shear-Wave Velocity Model from Empirical Site Amplification. *Bulletin of the Seismological Society of America*, 101(1):258–274.

Poggi, V., Edwards, B., and Fäh, D. (2012a). Characterizing the Vertical-to-Horizontal Ratio of Ground Motion at Soft-Sediment Sites. *Bulletin of the Seismological Society of America*, 102(6):2741–2756.

Poggi, V. and Fäh, D. (2010). Estimating Rayleigh wave particle motion from three-component array analysis of ambient vibrations. *Geophysical Journal International*, 180(1):251–267.

Poggi, V., Fäh, D., Burjánek, J., and Giardini, D. (2012b). The use of Rayleigh-wave ellipticity for site-specific hazard assessment and microzonation: application to the city of Lucerne, Switzerland. *Geophysical Journal International*, 188(3):1154–1172.

Roesset, J. (1970). Fundamentals of soil amplification. In Hansen, R. J., editor, *Seismic Design for Nuclear Power Plants*, pages 183–244. M.I.T. Press, Cambridge, Mass.

SIA (2014). *SIA 261 Einwirkungen auf Tragwerke*. Société suisse des ingénieurs et des architectes, Zurich, Switzerland.

Wathelet, M. (2008). An improved neighborhood algorithm: Parameter conditions and dynamic scaling. *Geophysical Research Letters*, 35(9):1–5.